Zitierweise: *Angew. Chem. Int. Ed.* **2024**, *63*, e202408163
doi.org/10.1002/anie.202408163

Mid-Infrared Photothermal Imaging

Structural Mapping of Protein Aggregates in Live Cells Modeling Huntington's Disease

Zhongyue Guo[+], Giulio Chiesa[+], Jiaze Yin, Adam Sanford, Stefan Meier, Ahmad S. Khalil, and Ji-Xin Cheng**

Abstract: While protein aggregation is a hallmark of many neurodegenerative diseases, acquiring structural information on protein aggregates inside live cells remains challenging. Traditional microscopy does not provide structural information on protein systems. Routinely used fluorescent protein tags, such as Green Fluorescent Protein (GFP), might perturb native structures. Here, we report a counter-propagating mid-infrared photothermal imaging approach enabling mapping of secondary structure of protein aggregates in live cells modeling Huntington's disease. By comparing mid-infrared photothermal spectra of label-free and GFP-tagged huntingtin inclusions, we demonstrate that GFP fusions indeed perturb the secondary structure of aggregates. By implementing spectra with small spatial step for dissecting spectral features within sub-micrometer distances, we reveal that huntingtin inclusions partition into a β-sheet-rich core and a α-helix-rich shell. We further demonstrate that this structural partition exists only in cells with the [*RNQ*$^+$] prion state, while [*rnq*$^-$] cells only carry smaller β-rich non-toxic aggregates. Collectively, our methodology has the potential to unveil detailed structural information on protein assemblies in live cells, enabling high-throughput structural screenings of macromolecular assemblies.

Introduction

Neurodegenerative diseases (NDs) share the common pathogenic mechanism of the accumulation of insoluble protein aggregates in the form of amyloid fibrils.[1] The formation of amyloid fibrils has been extensively studied in vitro, using conventional spectroscopic approaches[2] and biophysical characterizations.[3] Recent breakthrough in solid-state nuclear magnetic resonance spectroscopy (ssNMR)[4] and cryo-electron microscopy (cryo-EM)[5] led to determination of the atomic structure of amyloid fibrils. However, these in vitro studies on isolated fibrils do not take into account the complex environment in which aggregates form and elongate.

With the combinations of advanced microscopy[6] and genetic engineering,[7] fluorescent dyes[8] and fluorescent protein fusions have been used to study protein aggregates in cells. However, fluorescence microscopy alone does not provide structural information. Additionally, fluorescent proteins may lead to oligomerization or aggregation and further complicate the study.[9] Recently, cryo-electron tomography (cryo-ET) has been used to visualize the 3D structure of polyQ aggregates in situ in yeasts.[10] However, due to the complicated sample preparation, it only allows one snapshot in time.

Recently developed mid-infrared photothermal (MIP) microscopy,[11] also called optical photothermal infrared (O-PTIR) microscopy, opens a new way to structural studies of protein aggregates in live cells. MIP is a vibrational spectroscopic imaging technique, where a visible probe beam detects the photothermal effect induced by the mid-infrared (mid-IR) absorption. MIP simultaneously offers high spatial resolution with the visible probe, and rich chemical and structural information through the mid-infrared pump.[11] MIP imaging of subcellular structures in live cells has been successfully demonstrated in cancer cells and neurons.[11a,12] Moreover, MIP is a quantitative technique, particularly suitable to study the structure of protein

---

[*] Z. Guo,[+] Dr. G. Chiesa,[+] A. Sanford, S. Meier, Prof. A. S. Khalil, Prof. J.-X. Cheng
Department of Biomedical Engineering
Boston University
Boston MA 02215, USA
E-mail: gchiesa@bu.edu
jxcheng@bu.edu

Z. Guo,[+] J. Yin, Prof. J.-X. Cheng
Photonics Center
Boston University
Boston MA 02215, USA

Dr. G. Chiesa,[+] A. Sanford, Prof. A. S. Khalil
Biological Design Center
Boston University
Boston MA 02215, USA

J. Yin, Prof. J.-X. Cheng
Department of Electrical and Computer Engineering
Boston University
Boston MA 02215, USA

Prof. A. S. Khalil
Wyss Institute for Biologically Inspired Engineering
Harvard University
Boston MA 02215, USA

[+] These authors contributed equally.

aggregates. The amide I band from C=O stretching vibration of the protein backbone, correlates predictably to protein secondary structure. Amide I quantification is a conventional Fourier transform infrared (FTIR) application in vitro.[13] Using a commercial mIRage O-PTIR microscope, Oxana Klementieva and co-workers mapped β-sheet aggregation by intensity ratio of the 1630 cm^{-1} peak over the 1650 cm^{-1} peak in primary neurons cultured with synthetic Aβ (1–42) and showed structural polymorphic amyloid-β aggregates in AD transgenic neurons.[14] More recently, Jian Zhao et al. developed a fluorescence-guided bond-selective intensity diffraction tomography and achieved 3D visualization of intracellular tau fibrils by β-sheet structures in human cells seeded with extracted tau fibril.[15] Craig Prater et al. combined wide-field epi-fluorescence imaging with O-PTIR to perform spectroscopic analysis with the guidance of fluorescent amyloid tracers or amyloid-specific antibodies.[16] These studies were limited to aggregates in fixed cells or cryo-dried tissues, and full potential of MIP for structural analysis in single live cells remains untapped.

Here, we built a counter-propagating MIP system integrating fluorescence as guidance for spectral analysis. Additionally, we developed a wide-field fluorescence-detected MIP setup and harnessed fluorescent proteins as thermal reporters. We applied these systems to study live cells of a well-established eukaryotic model of protein aggregation,[17] where yeast cells express the highly aggregation-prone protein huntingtin, involved in Huntington's Disease.[18] We first confirmed β-sheet enrichment in aggregates in a high throughput manner. We performed MIP spectroscopy of fluorescent huntingtin aggregates and, using its spectral features, we learnt to achieve label-free identification of protein aggregates. In this way, we demonstrated that fluorescent protein fusion perturbs the structure of the aggregate. Next, multispectral MIP imaging revealed a spatial distribution of structurally distinct components within the inclusion, with a core highly enriched in β-sheet and a shell dominated by α-helix. Finally, we discovered that the structural partition is caused by the yeast prion [RNQ^+]. Altogether, our work demonstrates the potential of MIP micro-spectroscopy for structural dissection of protein aggregation processes in live single cells.

Results and Discussion

Principle of MIP Analysis of Protein Secondary Structure in Live Cells

Protein aggregation and, more specifically, amyloid formation are key hallmarks of multiple neurodegenerative diseases.[19] Disease-relevant proteins, such as the huntingtin protein in Huntington's Disease (HD), accumulate intracellularly into large, ordered structures. In vitro characterizations including NMR[20] and cryo-EM.[5b,21] revealed that these aggregates are organized in stacked polypeptides in β-sheet conformation, arranged in a fibril. However, it is challenging to translate these in vitro structural insights to the physiological and cellular state of protein aggregates. Cryo-EM[22] and PALM[23] have been used for structural analysis on aggregates within cells. These approaches either involve technically complex and expensive instruments, or are extremely labor intensive, preventing the analysis of multiple cells at a time.

Here, we showcase MIP microscopy as a new tool for structural analysis of protein aggregates in live cells (Figure 1A). We used live cell MIP imaging to study protein aggregates in their native environment, selecting yeast as a eukaryotic model of protein aggregation. Mid-infrared light provides rich chemical and structural information while the tightly focused visible probe light provides high spatial resolution that enables imaging of small protein aggregates inside live yeast cells. To acquire secondary structure information of protein aggregates, we focused on the amide I region of MIP. Amide I band vibration originates mainly from the C=O stretching in the peptide bonds of the protein backbone, directly associated to the backbone conformation. Amide I band is therefore most sensitive to protein secondary structure.[13b,d] Second derivative analysis and deconvolution of the amide I band reveal component peaks, which can be assigned to different secondary structures.[13a] MIP spectrum is faithful to the conventional IR absorption spectrum and allows quantitative measurements for structural study, as MIP intensity is linearly proportional to the number density of molecules.[11a] Therefore, MIP enables quantifiable secondary structural analysis of protein aggregates in live yeast cells.

The contrast mechanism of MIP imaging is explained in Figure 1B. Mid-infrared and visible laser beams are focused to the same spot. The selective absorption of mid-infrared causes a local temperature change. This photothermal effect origins from the vibrational transition after absorbing mid-infrared, and the subsequent nonradiative thermal relaxation.[11d] The sample is heated up locally by the ultrashort mid-infrared pulses, and gradually cools down through thermal diffusion. As fluorescence intensity decreases with increasing temperature, the photothermal effect can be detected by fluorescence.[24] Alternatively, this temperature change leads to thermal expansion and changes in refractive index, detectable by measuring the differential in scattering.[11a] Hence, detecting mid-infrared absorption by visible light greatly improves spatial resolution while providing rich chemical information.

A Eukaryotic Model of Protein Aggregation

The onset of neurodegenerative diseases is intimately associated with progressive degeneration of cell proteostasis.[25] Since the proteostasis machinery is conserved across eukaryotes, and *Saccharomyces cerevisiae*, also called budding yeast, is a fast-growing organism that enables introducing genetic manipulations simply, rapidly and inexpensively,[17] yeast is a particularly effective model system for neurodegenerative diseases.[26] We therefore leveraged a well-established model for protein aggregation in yeast[27] that recapitulates certain aspects of an hereditary neurodegenerative disease, called Huntington's Disease

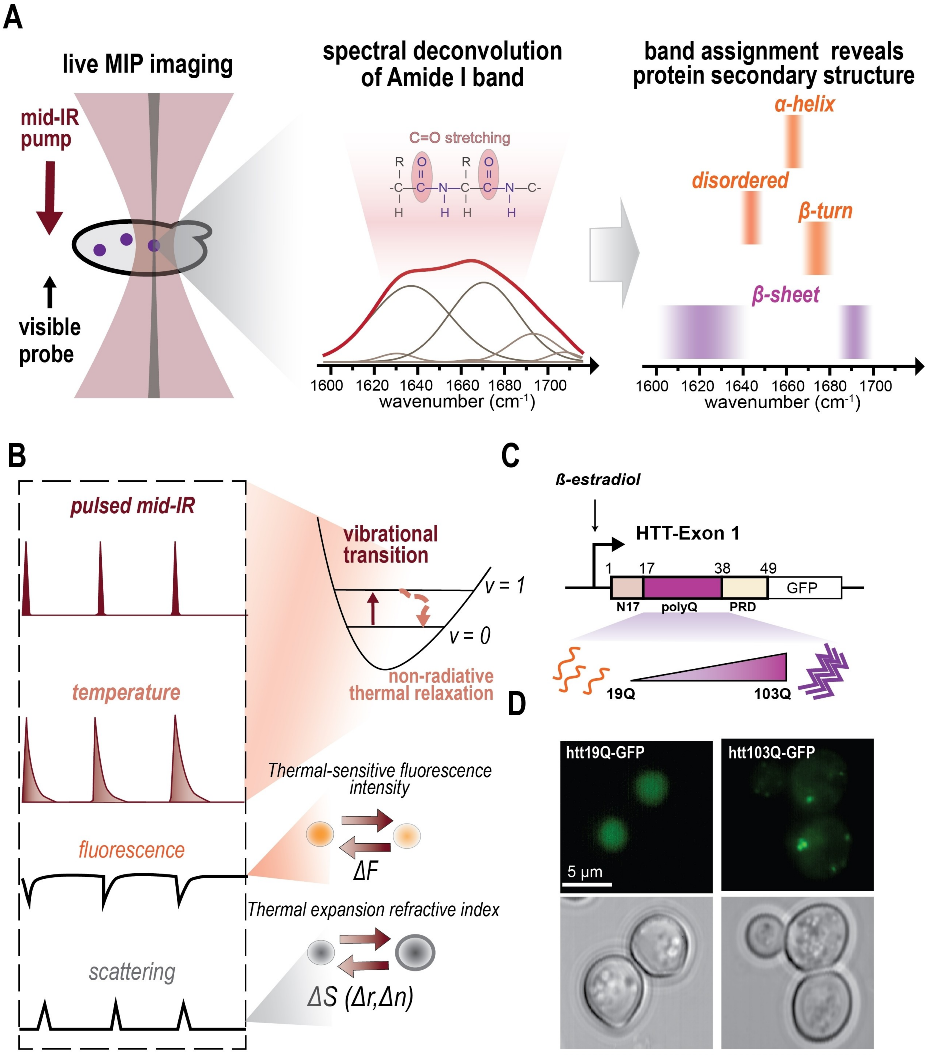

Figure 1. Secondary structure analysis of protein aggregates in live cells using a counter-propagating MIP system. (**A**) Concept of secondary structure analysis of protein aggregates in live cells. MIP imaging of live cells provides high spatial resolution, enabling the study of protein aggregates. Mid-IR absorption in the amide I band reveals protein secondary structures after deconvolution and component band assignment. (**B**) Representation of MIP detection: mid-IR pulses induce both fluorescence and scattering intensity changes. (**C**) β-estradiol inducible model for Huntington's Disease and protein aggregation in yeast. The sequence representation of HTT-Exon 1 is based on the exon 1 of htt protein (homo sapiens, UniProt P42858). PolyQ length predictably affects aggregation propensity. Low polyQ length (19Q) leads to soluble protein while high polyQ length (103Q) leads to protein aggregates. (**D**) Example of yeast cells expressing htt19Q-GFP show diffuse fluorescence, while cells expressing htt103Q-GFP show bright fluorescent foci indicating protein aggregates. Top: GFP fluorescence images. Bottom: corresponding transmission images. Scale bar: 5 μm.

(HD).[17] HD is caused by an expanded CAG trinucleotide repeat in the exon 1 of HTT gene, coding for huntingtin (htt) protein. The codon expansion leads to an abnormally long polyglutamine (polyQ) sequence in the mutant htt protein.[18] There is a well-established correlation between htt polyQ length, its propensity to form insoluble aggregates and the age of onset of the pathology: htt with larger polyQs is more aggregation prone and more toxic than short polyQ htt.[28]

In our system, exon 1 of protein huntingtin is conditionally overexpressed in a strain of *S. cerevisiae.* Overexpression of htt is known to cause aggregate formation, recognizable as puncta or foci by Thioflavin-S staining (or fluorescent foci, when the protein is tagged with a fluorophore).[29] The protein fragment formed by exon 1 retains both the intrinsically disordered 17 N-terminal amino acids (N17) and the proline-rich region (PRD) directly C-terminal to the polyQ. We considered a suite of mutants with polyQ length ranging from 19Q to 159Q. We then fused htt to a fluorescent protein (htt-FP). To regulate htt expression, we used a recently developed β-estradiol induction system (Figure 1C).[30] This orthogonal inducer for htt expression reduces confounding effects, such as metabolic changes due to change of carbon source and acute cytotoxicity.[31] We confirmed that htt-FP expressed in this setting would cause toxicity to cells, by monitoring growth curves of cells expressing either htt19Q-FP (non-aggregation prone) or htt103Q-FP (highly aggregation-prone). Indeed, htt103Q-FP imposes a visible growth defect to cells (Figure S1). We then monitored aggregate formation in yeast cells using fluorescence microscopy, by tracking the formation of bright fluorescent foci. Cells expressing soluble proteins (i.e. with low polyQ number, such as htt19Q-FP) would not accumulate fluorescent foci, but instead would show diffuse fluorescence,[27] whereas only cells overexpressing the aggregation-prone mutant of htt-FP would form clear foci (Figure 1D and S2). We used the formation of fluorescent foci as a guide for MIP analysis.

Wide-Field Fluorescence-Detected MIP Reveals β-Sheet Enrichment in htt Inclusions

The inherently high compatibility between MIP and fluorescence imaging enabled us to combine the rich chemical information of MIP with the high specificity of widely available fluorescent tools.[32] To characterize the secondary structure of protein aggregates, we initially fused htt protein with a green fluorescent protein (GFP). We first harnessed GFP as a sensitive sensor of temperature[24] in wide-field MIP. We describe the concept of high-throughput single-inclusion structural analysis by wide-field fluorescence-detected MIP in Figure S2. Briefly, wide-field fluorescence imaging of yeast cells enabled simultaneous analysis of tens of htt103Q-GFP inclusions within the mid-IR illumination area (~50 µm in diameter) while minimizing photobleaching of GFP.[24] The mid-IR pulses are optically chopped with 50 % duty cycle to produce IR on (‘hot’) and IR off (‘cold’) frames.

To distinguish structural properties of htt inclusions, we focused on the two extreme cases of a very low polyQ mutant (htt19Q-GFP), which is mostly soluble, and a very high polyQ mutant (htt103Q-GFP), which is very aggregation prone. We imaged yeast strains expressing each mutant respectively. As expected, the wide-field fluorescence images of yeast strains expressing htt19Q-GFP showed diffuse fluorescence while htt103Q-GFP showed bright foci (Figure 2A and Figure S3). Fluorescence videos were recorded with mid-IR excitation at 1658 cm^{-1} (representing α-helix) and at 1682 cm^{-1} (representing β-sheet) sequentially. The fluorescence intensity traces from representative htt19Q-GFP cell body and htt103Q-GFP foci showed clear modulation where hot frames (solid circle) had lower intensity compared with adjacent cold frames (open circle) (Figure 2B). Therefore, the MIP modulation depth (MD) was calculated as mid-IR induced change relative to the original fluorescence intensity for single htt19Q-GFP cell and htt103Q-GFP foci. htt103Q-GFP showed higher modulation at 1682 cm^{-1} while htt19Q-GFP showed higher modulation at 1658 cm^{-1}. Since the wide-field configuration is conducive

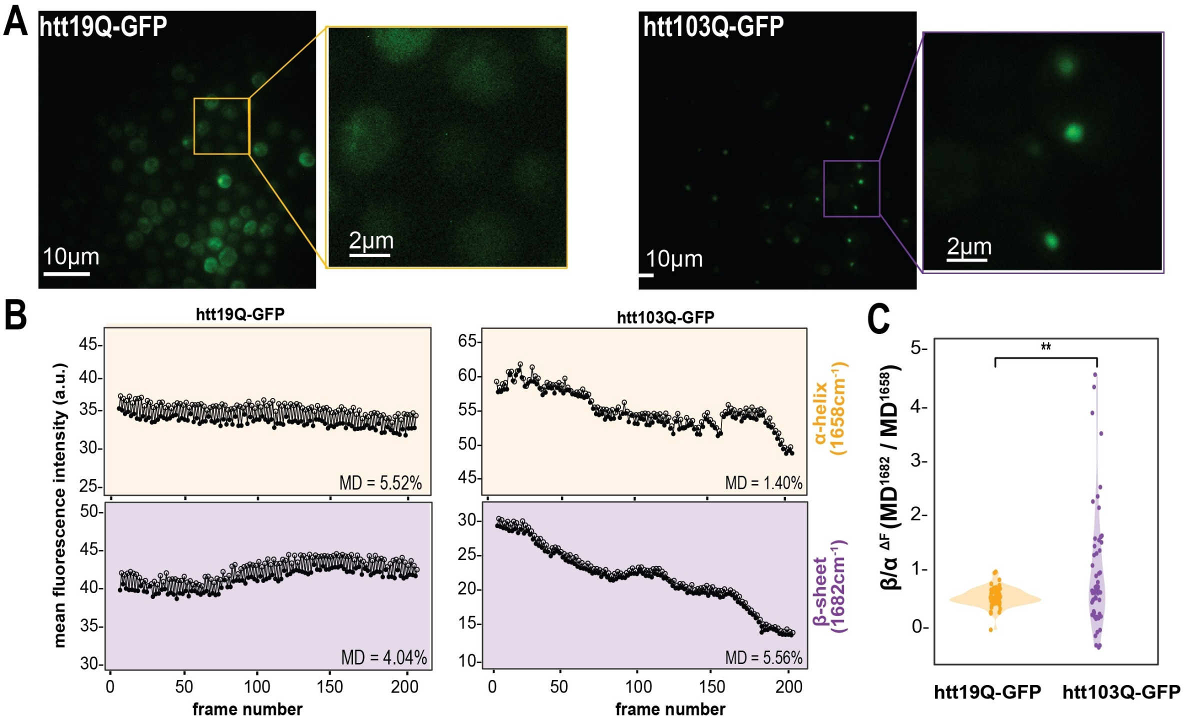

Figure 2. Wide-field fluorescence-detected MIP reveals β-sheet enrichment in fluorescently labeled protein inclusions with high throughput. (**A**) Representative wide-field fluorescence images and detail images of GFP fluorescent trace for htt19Q-GFP (left) and htt103Q-GFP (right). To successfully visualize htt19-GFP fluorescence, the camera gain for htt19Q-GFP was 20dB higher than that for htt103Q-GFP. Scale bars: 10 µm and 2 µm for detail inset. (**B**) Representative fluorescence intensity traces with mid-infrared at 1658 cm^{-1} for α-helix (top) and at 1682 cm^{-1} for β-sheet (bottom) for htt19Q-GFP cell (left) and htt103Q-GFP foci (right) at the center of the enlarged selection in images in (A). MD: modulation depth. (**C**) Statistical analysis of fluorescence modulation depth ratio at 1682 cm^{-1} over at 1658 cm^{-1} ($\beta/\alpha^{\Delta F}$) for htt19Q-GFP cell ($N=63$) and htt103Q-GFP foci ($N=55$). Unpaired pairwise t-test, $p=0.001$**.

to high throughput applications, we performed statistical analysis on the ratio between fluorescence modulation at 1682 cm^{-1} and at 1658 cm^{-1} ($\beta/\alpha^{\Delta F}$) and found a higher ratio for htt103Q-GFP compared with htt19Q-GFP (Figure 2C). This higher ratio indicates an enrichment of β-sheet structure in htt inclusions, which is consistent with in vitro representations of polyQ fibrils as amyloid fibrils formed by a core of interdigitates β-hairpins, or a stacked β-sheet.[33] Collectively, these data demonstrate that mid-IR-modulated fluorescence is able to reveal β-sheet enrichment in protein aggregates.

Fluorescence-Guided MIP Spectroscopy Dissects Secondary Structure of htt Inclusions

Having demonstrated that fluorescence intensity modulation by mid-infrared could reveal β-sheet enrichment of htt inclusions (Figure 2), we next switched to a counter-propagating point-scanning MIP system to harness fluorescence as a guidance to further explore the spectral features of htt inclusions. The schematic for fluorescence-guided MIP spectroscopy is shown in Figure 3A and Figure S4. Epi-fluorescence imaging was first performed to provide guidance for the intracellular location of protein inclusions. As the image was formed by raster scanning of the sample stage, single inclusions were targeted sequentially based on their center pixel positions by driving the piezo sample stage. Then, the MIP spectrum was acquired by continuously tuning the mid-IR wavenumbers.

We acquired a set of MIP spectra across protein inclusions (representative example in Figure 3B), by sequentially moving the stage to the center of fluorescent foci (bright green spots marked by purple crosses). The MIP spectrum showed significant shifts towards both low and high wavenumbers, instead of a broad amide I band. MIP spectrum in the amide I region was deconvoluted into multiple component peaks, whose centers were determined by the minima of the second derivative. Each peak could be assigned to different protein secondary structures based on their peak centers. The area under a component peak quantifies its relative contribution. To quantify the β-sheet enrichment, we calculated the β/α ratio as the ratio of the sum of β-sheet components peak area to that of α-helix, confirming that the core of htt aggregates (defined as the center of bright foci) is rich in β-sheet structure. A detailed description of MIP spectrum acquisition, processing, and structural analysis could be found in Experimental Details and Figure S5 to S10.

For validation, we measured MIP spectra by IR wavenumber tuning in both directions and noted no obvious heat accumulation due to infrared absorption for MIP spectra under our experimental settings (Figure S11). We also noticed that fixation leads to undetectable β-sheet enrichment in aggregates by MIP, possibly due to the effect of cross-link of proteins by paraformaldehyde (Figure S12 and Experimental Details).[34] Recently, a similar approach has been adapted to analyze amyloid content in fresh tissue biopsies. Interestingly, the authors also noticed discrepancies between fixed and live samples, similar to our observations (Figure S13), remarking the importance to transition to live cell imaging in studying amyloid fibers.[35]

β-Sheet Content Increases with PolyQ Length in htt Inclusions in Vivo

By performing full MIP scanning of fluorescent foci, we aimed at exploring how the structure of htt aggregates varies across polyQ variants. Studies in vitro demonstrated that polyQ proteins, given enough time, always converge in forming β-sheet rich (amyloid) fibrils at a rate dictated by the polyQ length.[36] This observation is in contrast with the well-established threshold effect seen in all polyQ diseases, where pathology eventually manifests exclusively when the polyQ is longer than a specific threshold (38 repeats for HD).[37] In yeast, it is well established that aggregation propensity of htt correlates with polyQ length,[27] but there is yet scarce information on a correlation between polyQ length and structural properties of the aggregates in their physiological state. Altogether, information on the structure of these aggregates is fragmented.[38] Hence, we were interested to study whether polyQ aggregates accumulating in cells invariably form β-sheet rich inclusions or if they vary in structural properties with polyQ length.

We expressed htt fusions with the fluorescent protein Crimson (httnQ-Cr) with variable polyQ length (respectively, 19Q, 49Q, 103Q and 159Q) and we analyzed yeast cells with MIP. In our analysis, 19Q showed a broad amide I band (Figure 3C orange), while representative spectra acquired from the fluorescent foci for Q length above the pathological threshold (159Q, 103Q and 49Q) showed a similar spectral change of increasing low- and high-wavenumber β-sheet (Figure 3C purples).

We further performed quantitative analysis of β/α ratio after amide I deconvolution. Interestingly, the analysis of β/α ratios of fluorescent traces of proteins with shorter polyQ could fit a sigmoidal curve, correlating polyQ length with β/α ratios (Figure 3D, Figure S13). In specific, htt-37Q showed an interesting intermediate state, with a lower β-sheet content within the inclusion than the above-threshold variants, but still higher than the background values obtained by scanning cells expressing htt-19Q, htt-26Q and htt-31Q.

Collectively, this data is consistent with a scenario where the maturation process involves a change in secondary structure from α-helical to β-sheet,[39] but once β-rich fibrils are formed,[33a] all acquire the same ultimate secondary structure: amyloid fibrils are a stable end point of a maturation process that occurs at rates dictated by polyQ length. Slower rates of aggregation enable cells to cope with accumulating aggregates, which explains the diverse β/α ratio across strains expressing short polyQs.[40]

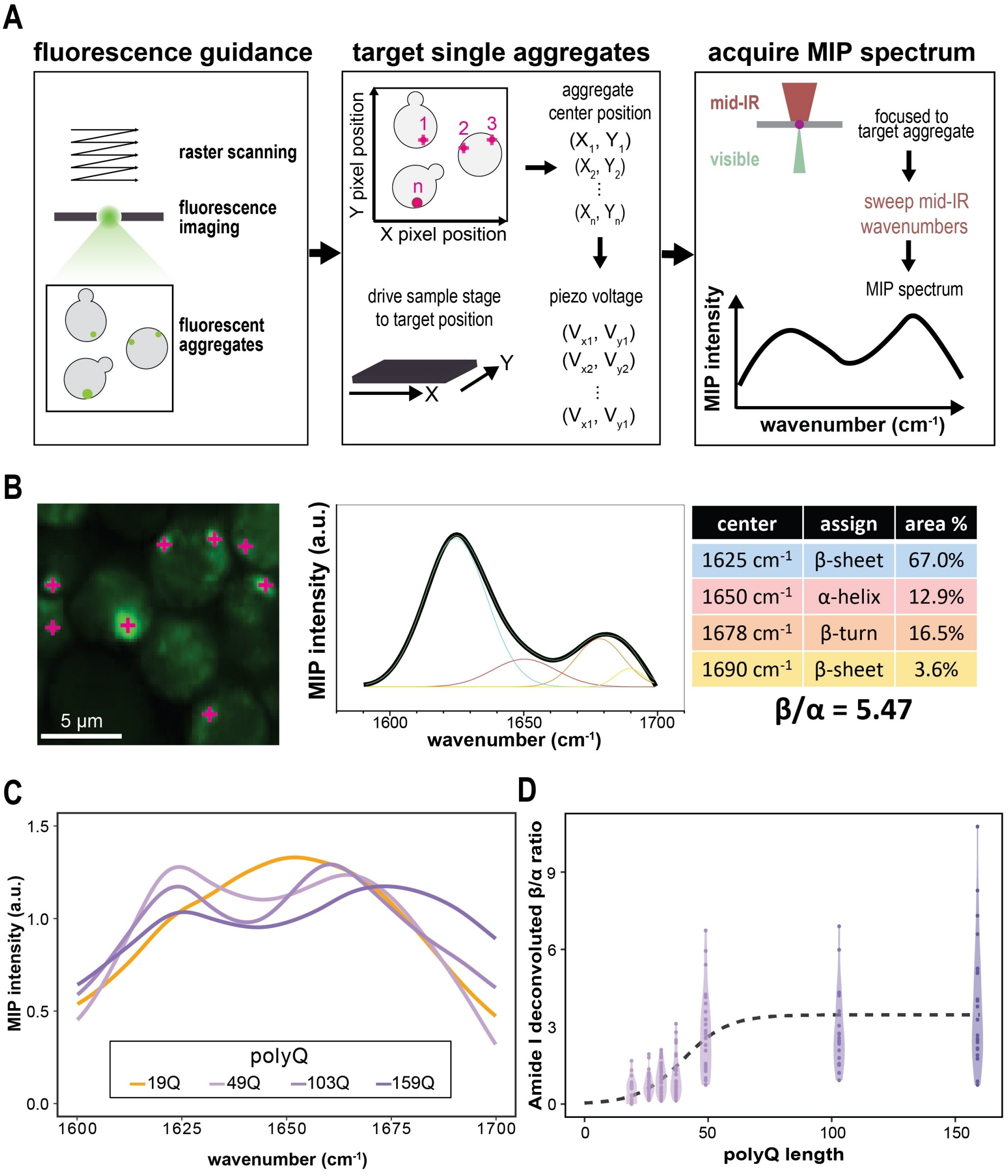

center	assign	area %
1625 cm^{-1}	β-sheet	67.0%
1650 cm^{-1}	α-helix	12.9%
1678 cm^{-1}	β-turn	16.5%
1690 cm^{-1}	β-sheet	3.6%

Figure 3. Fluorescence-guided MIP spectroscopy dissects spectral features of protein inclusions. (**A**) Schematic for fluorescence-guided MIP spectroscopy. Fluorescence imaging was first performed by raster scanning of the sample stage. To target single inclusions, the sample stage was driven by piezo voltage based on pixel positions of aggregate centers sequentially. The MIP spectra were acquired by continuously tuning the mid-IR wavenumbers. (**B**) A representative MIP spectrum of htt103Q-GFP aggregate acquired from fluorescent foci (bright green spots marked by purple crosses) and deconvoluted in amide I region into component peaks assigned to different secondary structures. β/α ratio was calculated by area under the component peaks. (**C**) Representative MIP spectra in amide I region acquired from 159Q, 103Q and 49Q aggregates under Crimson fluorescent guidance (shown in purple, darker shade indicates longer polyQ length), and from 19Q yeast cells (shown in orange). (**D**) β-sheet to α-helix ratio (β/α) quantified by amide I deconvolution for htt with multiple polyQ lengths (19Q, 26Q, 31Q, 37Q, 49Q, 103Q and 159Q). A nonlinear regression model fits a sigmoidal curve shown as dashed line. N > 20 per group.

Label-Free MIP Reveals Secondary Structure Perturbation in htt Aggregates Caused by Fusion of GFP

MIP can also scan the sample at multiple wavenumbers, mapping chemical information onto microscopic images. We argued that, once learned the spectral signature of protein aggregates, label-free analysis would be possible. To do this, we first tested live yeast cells expressing htt103Q-GFP, by sequentially acquiring fluorescence images (in green) and MIP images at 1658 cm^{-1} (representing α-helix, in red), 1628 cm^{-1} (representing low-wavenumber β-sheet, in cyan), and 1682 cm^{-1} (representing high-wavenumber β-sheet, in yellow), described in Figure 4A and Figure S14. We observed co-localization between GFP bright foci and strong MIP signals at both β-sheet wavenumbers (1628 and 1682 cm^{-1}). This result is compatible with the large literature of in vitro studies that describe polyQ fibers as stacked β-sheets.[33] Previously, protein content during cell division has

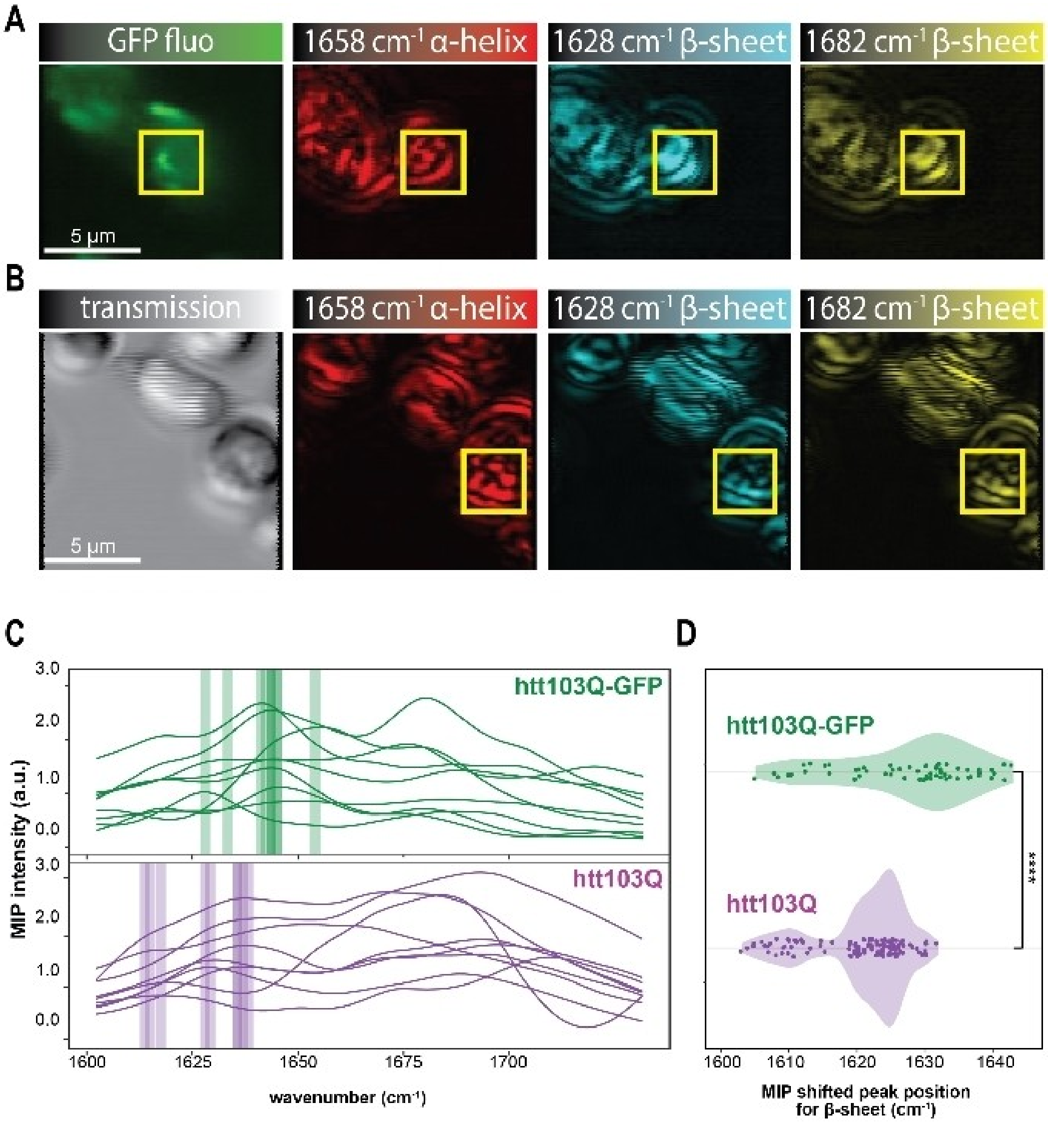

Figure 4. MIP detects structural perturbation caused by fusion of GFP. (**A**) Representative fluorescence images for GFP (green) and MIP images at 1658 cm^{-1} (α-helix, red), 1628 cm^{-1} (low-wavenumber β-sheet, cyan), and 1682 cm^{-1} (high-wavenumber β-sheet, yellow) for live yeasts expressing htt103Q-GFP. Scale bar: 5 µm. (**B**) Representative transmission image (gray) and MIP images at 1658 cm^{-1} (α-helix, red), 1628 cm^{-1} (low-wavenumber β-sheet, cyan), and 1682 cm^{-1} (high-wavenumber β-sheet, yellow) for live yeasts expressing htt103Q with no fluorescent tag. Scale bar: 5 µm. The yellow boxes identify the protein aggregate in (A) and (B). (**C**) Representative 9 MIP spectra in amide I region for htt103Q-GFP aggregates (top) with a shifted peak position for low-wavenumber β-sheet and htt103Q aggregates (bottom) with a further red-shifted peak position. (**D**) MIP shifted peak position for low-wavenumber β-sheet for htt103Q-GFP (N = 62) and htt103Q (N = 135) aggregates. Unpaired pairwise t-test, $p = 3.18 \times 10^{-6}$,****.

been monitored by a single wavenumber 1650 cm^{-1}.[12b] Here we show that multiple signature wavenumbers in the amide I region suffice to directly visualize the spatial distribution of different secondary structures of protein aggregates.

To validate that only htt103Q-GFP foci caused large differences between α-helical and β-sheet, we performed the same β/α ratio quantification on cells expressing htt103Q-GFP, cells carrying the same transgene, but without induction (103Q-DMSO), and cells expressing htt19Q-GFP. We reasoned that, given the disproportionate size of GFP (26.8 kDa) compared to htt19Q (11.4 kDa), htt19Q-GFP would represent essentially also a GFP control. We also compared β/α ratios of points within the fluorescent foci and points outside fluorescent foci in cells expressing htt103Q-GFP. Results are summarized in Figure S15.

We were aware that fusing htt to a fluorescent protein would likely affect its aggregation process, due to the relatively large size of the fluorescent protein compared to the htt, the intrinsic propensity of fluorescent proteins to oligomerize,[41] and their inherent structural signature.[42] A label-free modality of structural imaging would provide more faithful insights on the structure of aggregates in their physiological state. We therefore acquired MIP images at 1658, 1628 and 1682 cm^{-1} of cells expressing htt103Q with no fluorescent protein tag (Figure 4B). The chosen wavenumbers are representative of, respectively, α-helix, low-wavenumber β-sheet and high-wavenumber β-sheet. We scanned for areas characterized by high β-sheet and relatively low α-helix to identify htt103Q aggregates (Figure S16 to S18). We observed that the MIP spectra for htt103Q aggregates identified by structural features showed a further red shifted peak position for low-wavenumber β-sheet compared with htt103Q-GFP aggregates (Figure 4C). Statistical analysis showed a further red shift (i.e. even lower wavenumber) in the shifted peak position for β-sheet in htt103Q aggregates ($N=135$) compared with htt103Q-GFP aggregates ($N=62$) (Figure 4D).

This contribution of the fluorescent tag can be explained in two ways: first, their size, charge and propensity to aggregate can destabilize or influence the morphology of the aggregates. Second, GFP is distinctively enriched in β-sheets, hence potentially misleading an analysis based on secondary structure features. However, FTIR studies of purified proteins in vitro showed that native β-sheet proteins such as GFP have a shifted amide I peak position from 1630 to 1643 cm^{-1}, while amyloid fibrils present a distinctive amide I peak clustering between 1611 and 1630 cm^{-1}.[42] Therefore, discerning between GFP and amyloid spectral contributions should be possible, and analyzing the shift in amide I peak position provides specific information on the aggregate.[43]

Collectively, this data suggests that tagging aggregates with large fluorescent proteins produces confounding effects both by introducing more spectral contributions and by directly perturbing the structure of the aggregate itself. To the best of our knowledge, this is the first time that this spectral shift position difference due to fluorescent protein tagging was observed in protein aggregates in their physiological condition by MIP. Therefore, MIP offers an alternative approach to study protein aggregates based on spectral features and could potentially be used for label-free structural studies and diagnostics.

MIP Micro-Spectroscopy Reveals Structural Partitioning within Protein Aggregates

Interestingly, by examining the details of secondary structural distribution of htt103Q-GFP aggregate (represented in Figure 4A), we observed a spatial distribution of high intensities for α-helix wavenumber (1658 cm^{-1}) around the areas of high β-sheet intensity, where the α-rich region forms a hollow-like distribution around the β-rich region (Figure 5A). This suggests that htt aggregates are organized into a β-sheet enriched core, surrounded by a α-helix dominant outer layer. By tapping into the additional dimension of spectral information, we could detect the aggregation core enriched in β-sheet components, despite being of a lower size than the visible probe beam.[44]

The peculiar structural partitioning of α-rich and β-rich regions observed in Figure 5A motivated us to quantitatively explore spectral features throughout the protein aggregate. We hypothesized that this partition is intrinsic to the nature of htt aggregates. To do this, we recorded full MIP spectra sequentially along one direction across inclusion body with small spatial steps (Figure 5B and Figures S19). We noticed how spectra progressively shifted from α-rich to β-rich and back to α-rich along the cross-section, as showed by the variation in β/α ratio along the axis (Figure 5B and Figures S19 to S21). We acquired MIP spectra from $x=-100$, 0, and $+75$ nm relative positions and quantified the β/α ratio. The center showed the highest β/α of 5.47 and β/α decreased to 1.17 ($x=+75$ nm) and 1.07 ($x=-100$ nm) away from the center. This analysis validated the observation in Figure 5A.

To exclude potential contribution of GFP to this partitioning, we performed small step full MIP spectra also on htt103Q aggregates (devoid of GFP fusion). We plotted the X-dimension and Y-dimension line profile for this identified aggregate at 1658 cm^{-1}, 1628 cm^{-1} and 1682 cm^{-1} and observed a center with high β-sheet and corresponding dip in α-helix (Figure 5C). Once we acquired MIP spectra with small spatial steps, we observed an even higher β-sheet to α-helix ratio (β/α) of 10.79 at the aggregation center as well as a more drastic drop in β/α ratios 25 and 12.5 nm away from the center (Figure 5D and Figure S22), suggesting that this spatial partitioning is not caused by GFP.

Collectively, we revealed the spatial distribution of structurally distinct components within the protein inclusion through direct visualization by multispectral MIP imaging at signature wavenumbers. Additionally, by moving along the inclusion body with nanometer sized spatial steps, we revealed different degrees of relative contribution of the β-sheet core to the acquired MIP spectra, causing drastic spectral changes within nanometer distances below the conventional optical diffraction limit. This demonstrates how performing quantitative analysis of full MIP spectra with nanometer spatial steps can finely dissect the protein aggregate into structurally distinct regions.

It has been proposed that the first step of htt aggregation is the formation of liquid droplets which then evolve into their fibrillar state, both in vitro[45] and in vivo.[46] Our results of an enrichment in α-helical content at the edges of the β-sheet rich region suggest proteins in different secondary structures partition within the aggregate, and provides a structural connotation to previous observations of a core–shell organization in htt aggregates.[46b,c] In this scenario, the fibrillar and rigid core has β-sheet conformation, while the more dynamic and liquid shell is characterized by a preponderance of α-helical structure. This phenomenon could have two possible explanations: (i) given the polymorphic nature of polyQs[47] and the relatively high helical content of htt exon 1,[48] it is conceivable that htt fibrils maturate from within the condensate, giving rise to the partition of structures we observed, where amyloid fibrils emerge from α-rich non-fibrillar condensate.[49] Alternatively, (ii) inclusions are a heterogeneous composition of multiple protein species, where fibrils nucleate in the center of the inclusion and partition from other proteins,[46b] whereas the shell of the inclusion is more promiscuous.[46c] Indeed, we hypothesized that this structural heterogeneity is a consequence of the heterogeneous composition of the inclusion.

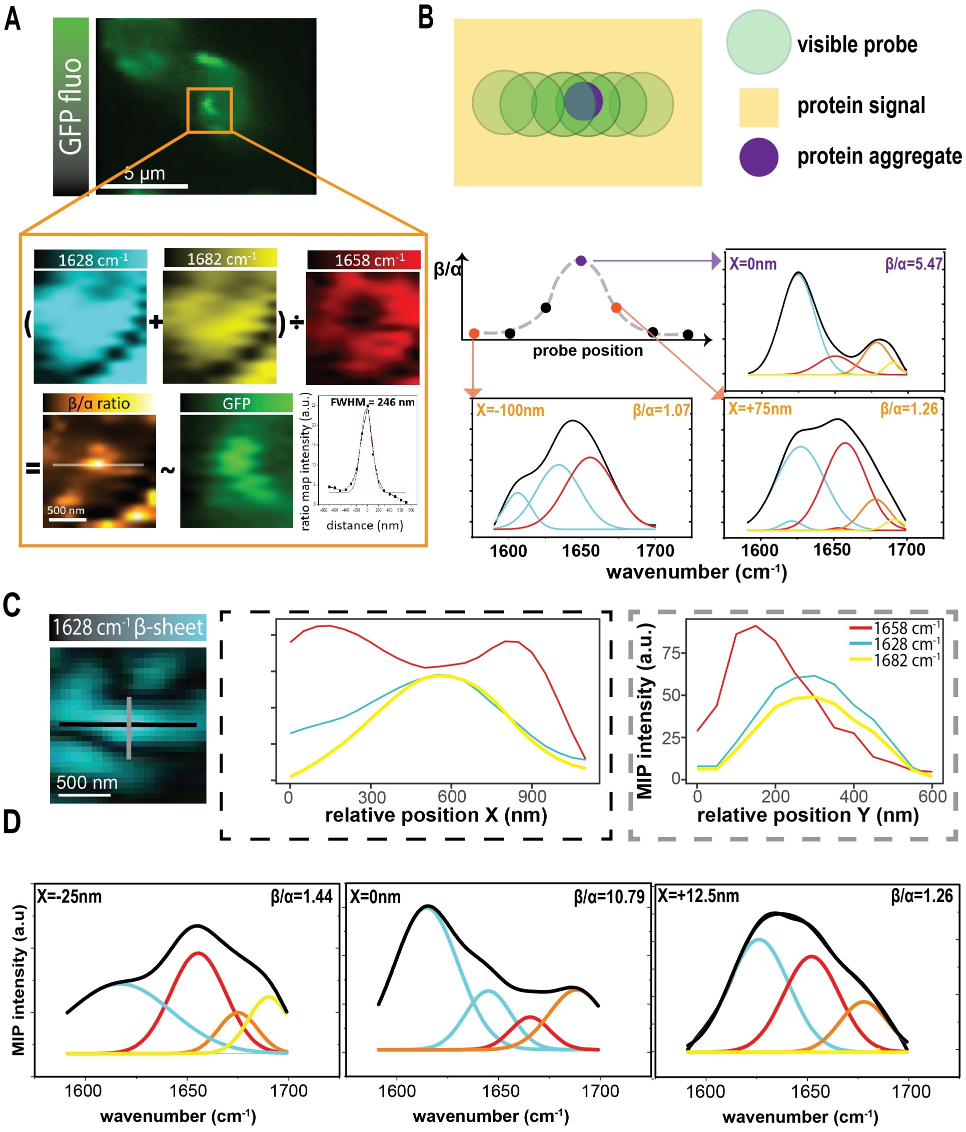

Figure 5. MIP resolves structural partitioning of htt aggregates at the sub-micrometer scale. (**A**) Detailed spatial distribution of htt103Q-GFP aggregate revealed a β-sheet enriched core surrounded by a α-helix dominant outer layer. Ratio map agreed with fluorescence, and full width half maximum (FWHM) estimated on the ratio showed an improvement compared with the theoretical resolution limit. (**B**) MIP spectra with small spatial steps across the β-sheet enriched core revealed drastic changes in β-sheet enrichment for htt103Q-GFP aggregate with MIP spectra acquired at relative positions $x=-100$, 0, $+75$ nm in amide I region (overall spectra in black, component peaks colored) and quantified β-sheet to α-helix ratios (β/α) for htt103Q aggregate: (**C**) X-dimension (left) and Y-dimension (right) line profile of identified aggregate at 1658 cm^{-1} (red), 1628 cm^{-1} (cyan) and 1682 cm^{-1} (yellow) and (**D**) MIP spectra acquired at relative positions $x=-25$, 0, $+12.5$ nm in amide I region (overall spectra in black, component peaks colored) and quantified β-sheet to α -helix ratios (β/α) for htt103Q-GFP aggregates.

MIP Micro-Spectroscopy Reveals the Influence of the Rnq1 Prion on the Structural Properties of htt Aggregates

The prion protein Rnq1 is known to aggregate in a prion form known as $[RNQ^{+}]$. Rnq1 has unknown functions when soluble, but, in its prion form, it facilitates formation of other prions, such as $[PSI^{+}]$ (prion form of the protein Sup35).[50] It is also well-known that the $[RNQ^{+}]$ state can facilitate htt aggregation in *S. cerevisiae* and induces toxicity.[51] There is also evidence of co-localization Rnq1 protein within htt inclusions by fluorescent microscopy.[52] Moreover, recent work has described the formation of dynamic condensates by htt in yeast,[45,53] and condensates formed by aggregation-prone proteins follow a maturation process where they progressively transition from dynamic liquid-like droplets into solid-like fibrillary structures from within the droplet.[49a,54] We therefore hypothesize that the structural partitioning described in Figure 5 is caused by the heterogeneous condensation of htt with Rnq1 protein, which then nucleates the formation of fully fibrillary aggregates.

To investigate this, we used an optogenetic approach to induce polyQ aggregation in $[rnq^{-}]$ cells that would otherwise not form consistent polyQ aggregates (Figure 6A).[55] Here, htt was fused to mCherry and Cry2 (htt43Q-Cry2-

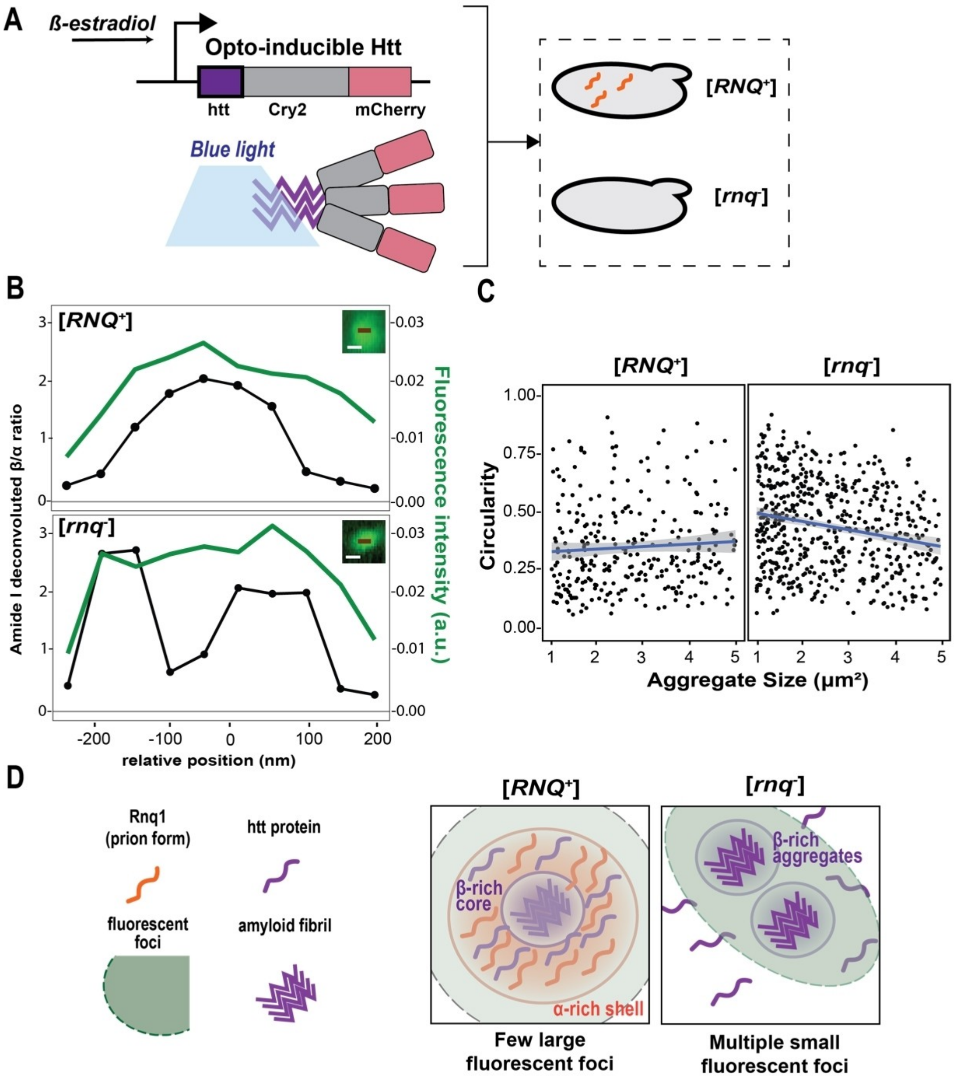

Figure 6. MIP detects perturbations caused by the prion Rnq1 on the structural properties of htt aggregates. (**A**) Experimental approach to study the role of prion Rnq1 in htt aggregation. In both $[RNQ^+]$ and $[rnq-]$ cells, β-estradiol induces expression of recombinant htt43Q-Cry2-mCherry and blue light stimulates nucleation of the aggregate (**B**) β/α ratio plot along the line of protein aggregates overlaid with fluorescence intensity for $[RNQ^+]$ strain (top) and $[rnq^-]$ strain (bottom). Inset: mCherry fluorescence images in green, scale bar 500 nm. (**C**) Circularity of fluorescent foci against the aggregate size in $[RNQ^+]$ (left) and $[rnq^-]$ strains. Each dot represents single fluorescent foci. Blue line shows linear fitting. N = 283 for $[RNQ^+]$ and N = 546 for $[rnq^-]$ (**D**) Schematic representation of htt aggregates in $[RNQ^+]$ and $[rnq^-]$ cells: the prion form of Rnq1 protein (orange) nucleates htt aggregation (purple), by forming α-rich aggregates, from which amyloid (β-rich) fibrils maturate, leading to one large fluorescent foci. In $[rnq^-]$ cells, aggregation of htt (when possible) follows a separate aggregation kinetics than in $[RNQ^+]$ cells, bypassing the α-rich nucleation step, leading to multiple smaller and β-rich fluorescent foci.

mCherry). Cry2 is a protein found in *Arabidopsis thaliana* that forms oligomers in response to blue light stimulation and is widely used in optogenetics experiments.[56] We generated yeast strains containing inducible versions of htt43Q-Cry2-mCherry in either a $[RNQ^+]$ or $[rnq^-]$ background. To incorporate blue light stimulation into our microscope, we used the powerful illumination lamp in the MIP microscope and added a band pass filter (480/10 nm) before focusing the blue light on to the sample using the IR objective.

We observed formation of new fluorescent foci after blue light stimulation in estradiol-induced Cry2-mCherry cells in both $[rnq^-]$ and $[RNQ^+]$ backgrounds (Figure S23). In $[rnq^-]$ cells, htt43Q-Cry2-mCherry formed significantly more inclusions after 5 minutes of blue light stimulation (Figure S24). No difference in the β/α ratio from MIP spectra was observed between htt43Q-Cry2-mCherry and htt49Q-Crimson in $[RNQ^+]$ strains (Figure S25), suggesting that Cry2 does not perturb the type of aggregates formed, but only induces their nucleation.

We then compared MIP spectra and β/α ratios across the htt43Q-Cry2-mCherry aggregates in $[RNQ^+]$ and in $[rnq^-]$ strains. MIP analysis of fluorescent foci in $[RNQ^+]$ showed symmetric single peaks in the β/α plots of their cross-section (with a 50 nm step), as expected, whereas large bright fluorescent foci found in $[rnq^-]$ presented fluctuations with multiple peaks in the β/α plots of their cross-section (Figure 6B and Figure S26). This suggested the presence of multiple smaller aggregates close in space, but below the diffraction limit.

To explain our observations, we hypothesized that, if this scenario was true, large bright foci in [RNQ^+] would have a round shape, whereas large bright foci in [rnq^-] would have lower circularity due to the combined fluorescence of multiple sources close in space. Hence, circularity of foci should scale with size in the [rnq^-] background, but not scale in the [RNQ^+] background. To validate this, we plotted foci circularity against particle size of inclusions within cells. As expected, particle size had an inverse correlation with circularity value in inclusions found in [rnq^-], whereas those found in [RNQ^+] had no variation of circularity across sizes (Figure 6C). Finally, we measured cell growth curves in presence of blue light for yeast cells expressing htt43Q-Cry2-mCherry in both backgrounds, Interestingly, growth in [RNQ^+] was slower compared with [rnq^-] strains (Figure S27), confirming that the presence of the prion form of Rnq1 protein is associated with toxicity in this cellular model of Huntington's Disease.[55]

Collectively, we demonstrate that MIP spectroscopy detects ultrastructural perturbations caused by the prion form of Rnq1 to htt aggregates. Our results suggest that Rnq1 is not only associated with the nucleation of htt aggregates, but also influences their physical and structural properties. We propose that, when nucleated by Rnq1 prion, htt aggregates are initially dynamic, mostly composed of proteins in α-helical conformation and with properties close to those of liquid droplets,[45] but then quickly progress into more rigid and fibrillary structures. The core–shell distribution is therefore reminiscent of this transition.[49a] Conversely, in absence of other prions, htt forms smaller, exclusively β-sheet and potentially non-miscible aggregates, suggesting the nucleation step is followed directly by fibril formation (Figure 6D).

Conclusions

This work showcases a comprehensive set of MIP microspectroscopic methods for structural and functional mapping of macromolecular assemblies in live cells, and provides a proof-of-concept of this application in the context of huntingtin aggregation. By using MIP, we obtained label-free structural information on huntingtin aggregates, as well as revealed, for the first time, a structural partition within the inclusion. Our MIP microscopy method can be readily expanded on multiple types of macromolecular assemblies, such as ribonucleoprotein droplets, and stress granules, as well as live mammalian cells, such as neurons. Additionally, more nuanced insights from the MIP spectra could be explored, including differentiating between parallel and anti-parallel β-sheets, or between intermolecular and intramolecular β-sheets. Finally, the structural mapping by multispectral MIP imaging could also be developed for studying the temporal dynamics of structural changes in spatial distribution.

Conflict of Interest

The authors declare no conflict of interest.

Data Availability Statement

The data that support the findings of this study are openly available in zenodo at 10.5281/zenodo.1002868881/zenodo.10028688, reference number 10028688.

Keywords: Vibrational Spectroscopy · Protein Aggregation · Secondary Structure · Synthetic Biology · Huntington's Disease

[1] a) M. S. Forman, J. Q. Trojanowski, V. M. Lee, *Nat. Med.* **2004**, *10*, 1055–1063; b) P. Sweeney, H. Park, M. Baumann, J. Dunlop, J. Frydman, R. Kopito, A. McCampbell, G. Leblanc, A. Venkateswaran, A. Nurmi, R. Hodgson, *Transl Neurodegener* **2017**, *6*, 6.

[2] a) B. Martial, T. Lefèvre, M. Auger, *Biophysical Reviews* **2018**, *10*, 1133–1149; b) M. F. Pignataro, M. G. Herrera, V. I. Dodero, *Molecules* **2020**, *25*.

[3] a) C. Goldsbury, U. Baxa, M. N. Simon, A. C. Steven, A. Engel, J. S. Wall, U. Aebi, S. A. Muller, *J. Struct. Biol.* **2011**, *173*, 1–13; b) J. Adamcik, R. Mezzenga, *Curr. Opin. Colloid Interface Sci.* **2012**, *17*, 369–376; c) F. S. Ruggeri, T. Sneideris, M. Vendruscolo, T. P. J. Knowles, *Arch. Biochem. Biophys.* **2019**, *664*, 134–148.

[4] a) B. H. Meier, R. Riek, A. Bockmann, *Trends Biochem. Sci.* **2017**, *42*, 777–787; b) A. Loquet, N. El Mammeri, J. Stanek, M. Berbon, B. Bardiaux, G. Pintacuda, B. Habenstein, *Methods* **2018**, *138–139*, 26–38.

[5] a) L. Gremer, D. Schölzel, C. Schenk, E. Reinartz, J. Labahn, R. B. Ravelli, M. Tusche, C. Lopez-Iglesias, W. Hoyer, H. Heise, *Science* **2017**, *358*, 116–119; b) R. Guerrero-Ferreira, N. M. Taylor, D. Mona, P. Ringler, M. E. Lauer, R. Riek, M. Britschgi, H. Stahlberg, *eLife* **2018**, *7*; c) Y. Li, C. Zhao, F. Luo, Z. Liu, X. Gui, Z. Luo, X. Zhang, D. Li, C. Liu, X. Li, *Cell Res* **2018**, *28*, 897–903.

[6] a) G. S. Kaminski Schierle, S. van de Linde, M. Erdelyi, E. K. Esbjorner, T. Klein, E. Rees, C. W. Bertoncini, C. M. Dobson, M. Sauer, C. F. Kaminski, *J. Am. Chem. Soc.* **2011**, *133*, 12902–12905; b) A. Kitamura, M. Kinjo, *Int. J. Mol. Sci.* **2018**, *19*.

[7] a) G. A. Newby, S. Kiriakov, E. Hallacli, C. Kayatekin, P. Tsvetkov, C. P. Mancuso, J. M. Bonner, W. R. Hesse, S. Chakrabortee, A. L. Manogaran, S. W. Liebman, S. Lindquist, A. S. Khalil, *Cell* **2017**, *171*, 966–979e918; b) M. Pereira, D. Tome, A. S. Domingues, A. S. Varanda, C. Paulo, M. A. S. Santos, A. R. Soares, *Biotechnol. J.* **2018**, *13*, e1700676; c) Y. Zeng, A. M. Jones, E. E. Thomas, B. Nassif, J. J. Silberg, L. Segatori, *ACS Synth. Biol.* **2018**, *7*, 2126–2138; d) G. Chiesa, S. Kiriakov, A. S. Khalil, *BMC Biol.* **2020**, *18*, 35.

[8] a) B. Frieg, L. Gremer, H. Heise, D. Willbold, H. Gohlke, *Chem. Commun. (Camb.)* **2020**, *56*, 7589–7592; b) S. Navarro, S. Ventura, *Biotechnol. J.* **2014**, *9*, 1259–1266.

[9] L. M. Costantini, E. L. Snapp, *DNA Cell Biol.* **2013**, *32*, 622–627.

[10] a) F. J. B. Bauerlein, I. Saha, A. Mishra, M. Kalemanov, A. Martinez-Sanchez, R. Klein, I. Dudanova, M. S. Hipp, F. U. Hartl, W. Baumeister, R. Fernandez-Busnadiego, *Cell* **2017**, *171*, 179–187e110; b) A. Gruber, D. Hornburg, M. Antonin, N. Krahmer, J. Collado, M. Schaffer, G. Zubaite, C. Luchtenborg, T. Sachsenheimer, B. Brugger, M. Mann, W. Baumeister, F. U.

Hartl, M. S. Hipp, R. Fernandez-Busnadiego, *Proc. Natl. Acad. Sci. USA* **2018**, *115*, E3446–E3453.

[11] a) D. Zhang, C. Li, C. Zhang, M. N. Slipchenko, G. Eakins, J.-X. Cheng, *Sci. Adv.* **2016**, *2*, e1600521; b) Z. Li, K. Aleshire, M. Kuno, G. V. Hartland, *J. Phys. Chem. B* **2017**, *121*, 8838–8846; c) Y. Bai, J. Yin, J.-X. Cheng, *Sci. Adv.* **2021**, *7*, eabg1559; d) Q. Xia, J. Yin, Z. Guo, J. X. Cheng, *J. Phys. Chem. B* **2022**, *126*, 8597–8613.

[12] a) Y. Bai, D. Zhang, C. Li, C. Liu, J. X. Cheng, *J. Phys. Chem. B* **2017**, *121*, 10249–10255; b) J. M. Lim, C. Park, J. S. Park, C. Kim, B. Chon, M. Cho, *J. Phys. Chem. Lett.* **2019**, *10*, 2857–2861; c) D. Zhang, L. Lan, Y. Bai, H. Majeed, M. E. Kandel, G. Popescu, J. X. Cheng, *Light-Sci. Appl.* **2019**, *8*, 116; d) A. Spadea, J. Denbigh, M. J. Lawrence, M. Kansiz, P. Gardner, *Anal. Chem.* **2021**, *93*, 3938–3950.

[13] a) J. Kong, S. Yu, *Acta Biochim. Biophys. Sin.* **2007**, *39*, 549–559; b) A. Barth, *Biochim. Biophys. Acta* **2007**, *1767*, 1073–1101; c) M. J. Baker, J. Trevisan, P. Bassan, R. Bhargava, H. J. Butler, K. M. Dorling, P. R. Fielden, S. W. Fogarty, N. J. Fullwood, K. A. Heys, *Nature protocols* **2014**, *9*, 1771–1791; d) H. Yang, S. Yang, J. Kong, A. Dong, S. Yu, *Nat. Protoc.* **2015**, *10*, 382–396.

[14] O. Klementieva, C. Sandt, I. Martinsson, M. Kansiz, G. K. Gouras, F. Borondics, *Adv. Sci.* **2020**, *7*, 1903004.

[15] J. Zhao, L. Jiang, A. Matlock, Y. Xu, J. Zhu, H. Zhu, L. Tian, B. Wolozin, J.-X. Cheng, *Light: Science & Applications* **2023**, *12*, 147.

[16] C. Prater, Y. Bai, S. C. Konings, I. Martinsson, V. S. Swaminathan, P. Nordenfelt, G. Gouras, F. Borondics, O. Klementieva, *J. Med. Chem.* **2023**, *66*, 2542–2549.

[17] L. Miller-Fleming, F. Giorgini, T. F. Outeiro, *Biotechnol. J.* **2008**, *3*, 325–338.

[18] G. P. Bates, R. Dorsey, J. F. Gusella, M. R. Hayden, C. Kay, B. R. Leavitt, M. Nance, C. A. Ross, R. I. Scahill, R. Wetzel, E. J. Wild, S. J. Tabrizi, *Nat Rev Dis Primers* **2015**, *1*, 15005.

[19] a) F. Chiti, C. M. Dobson, *Annu. Rev. Biochem.* **2017**, *86*, 27–68; b) A. P. Marsh, *Neurological Research and Practice* **2019**, *1*, 1–7; c) A. Sturrock, B. R. Leavitt, *Journal of geriatric psychiatry and neurology* **2010**, *23*, 243–259; d) S. Chen, F. A. Ferrone, R. Wetzel, *Proc. Natl. Acad. Sci. USA* **2002**, *99*, 11884–11889; e) K. Świtońska-Kurkowska, B. Krist, J. Delimata, M. Figiel, *Frontiers in Cell and Developmental Biology* **2021**, *9*, 642773.

[20] M. A. Wälti, F. Ravotti, H. Arai, C. G. Glabe, J. S. Wall, A. Böckmann, P. Güntert, B. H. Meier, R. Riek, *Proc. Natl. Acad. Sci. USA* **2016**, *113*, E4976–E4984.

[21] M. Kollmer, W. Close, L. Funk, J. Rasmussen, A. Bsoul, A. Schierhorn, M. Schmidt, C. J. Sigurdson, M. Jucker, M. Fändrich, *Nat. Commun.* **2019**, *10*, 4760.

[22] A. W. Fitzpatrick, B. Falcon, S. He, A. G. Murzin, G. Murshudov, H. J. Garringer, R. A. Crowther, B. Ghetti, M. Goedert, S. H. Scheres, *Nature* **2017**, *547*, 185–190.

[23] F. J. Bäuerlein, R. Fernández-Busnadiego, W. Baumeister, *Trends Cell Biol.* **2020**, *30*, 951–966.

[24] Y. Zhang, H. Zong, C. Zong, Y. Tan, M. Zhang, Y. Zhan, J.-X. Cheng, *J. Am. Chem. Soc.* **2021**, *143*, 11490–11499.

[25] C. López-Otín, M. A. Blasco, L. Partridge, M. Serrano, G. Kroemer, *Cell* **2013**, *153*, 1194–1217.

[26] V. Khurana, S. Lindquist, *Nat. Rev. Neurosci.* **2010**, *11*, 436–449.

[27] S. Krobitsch, S. Lindquist, *Proc. Natl. Acad. Sci. USA* **2000**, *97*, 1589–1594.

[28] a) S. Chen, F. A. Ferrone, R. Wetzel, *Proc. Natl. Acad. Sci. USA* **2002**, *99*, 11884–11889; b) I. H. Kratter, S. Finkbeiner, *Neuron* **2010**, *67*, 897–899; c) E. S. Blum, A. R. Schwendeman, S. Shaham, *Trends Cell Biol.* **2013**, *23*, 168–174.

[29] a) L. Z. Osherovich, J. S. Weissman, *Cell* **2001**, *106*, 183–194; b) A. B. Meriin, X. Zhang, X. He, G. P. Newnam, Y. O. Chernoff, M. Y. Sherman, *The Journal of cell biology* **2002**, *157*, 997–1004.

[30] A. Sanford, S. Kiriakov, A. S. Khalil, *ACS Synth. Biol.* **2022**, *11*, 3912–3920.

[31] A. Ocampo, A. Barrientos, *BioTechniques* **2008**, *45*, vii–xiv.

[32] Y. Bai, Z. Guo, F. C. Pereira, M. Wagner, J.-X. Cheng, *Anal. Chem.* **2022**.

[33] a) C. L. Hoop, H.-K. Lin, K. Kar, G. Magyarfalvi, J. M. Lamley, J. C. Boatz, A. Mandal, J. R. Lewandowski, R. Wetzel, P. C. van der Wel, *Proc. Natl. Acad. Sci. USA* **2016**, *113*, 1546–1551; b) J. C. Boatz, T. Piretra, A. Lasorsa, I. Matlahov, J. F. Conway, P. C. van der Wel, *J. Mol. Biol.* **2020**, *432*, 4722–4744.

[34] a) J. T. Mason, T. J. O'leary, *Journal of Histochemistry Cytochemistry* **1991**, *39*, 225–229; b) V. Zohdi, D. R. Whelan, B. R. Wood, J. T. Pearson, K. R. Bambery, M. J. Black, *PLoS One* **2015**, *10*, e0116491.

[35] N. Gvazava, S. C. Konings, E. Cepeda-Prado, V. Skoryk, C. H. Umeano, J. Dong, I. A. Silva, D. R. Ottosson, N. D. Leigh, D. E. Wagner, *J. Am. Chem. Soc.* **2023**.

[36] K. Kar, M. Jayaraman, B. Sahoo, R. Kodali, R. Wetzel, *Nat. Struct. Mol. Biol.* **2011**, *18*, 328–336.

[37] A. Adegbuyiro, F. Sedighi, A. W. T. Pilkington, S. Groover, J. Legleiter, *Biochemistry* **2017**, *56*, 1199–1217.

[38] A. Gruber, D. Hornburg, M. Antonin, N. Krahmer, J. Collado, M. Schaffer, G. Zubaite, C. Lüchtenborg, T. Sachsenheimer, B. Brügger, *Proc. Natl. Acad. Sci. USA* **2018**, *115*, E3446–E3453.

[39] R. Mishra, M. Jayaraman, B. P. Roland, E. Landrum, T. Fullam, R. Kodali, A. K. Thakur, I. Arduini, R. Wetzel, *J. Mol. Biol.* **2012**, *415*, 900–917.

[40] M. S. Hipp, S.-H. Park, F. U. Hartl, *Trends Cell Biol.* **2014**, *24*, 506–514.

[41] a) Y. Jiang, S. E. Di Gregorio, M. L. Duennwald, P. Lajoie, *Traffic* **2017**, *18*, 58–70; b) T. Ochiishi, K. Yamasaki, K. Hirose, A. Kitamura, T. Urabe, N. Hattori, M. Kinjo, T. Ebihara, H. Shimura, *Sci. Rep.* **2016**, *6*, 1–15.

[42] G. Zandomeneghi, M. R. Krebs, M. G. McCammon, M. Fandrich, *Protein Sci.* **2004**, *13*, 3314–3321.

[43] a) R. Sarroukh, E. Goormaghtigh, J.-M. Ruysschaert, V. Raussens, *Biochimica et Biophysica Acta (BBA)-Biomembranes* **2013**, *1828*, 2328–2338; b) J. Kubelka, T. A. Keiderling, *J. Am. Chem. Soc.* **2001**, *123*, 12048–12058.

[44] a) Y. Phal, L. Pfister, P. S. Carney, R. Bhargava, *J. Phys. Chem. C* **2022**, *126*, 9777–9783; b) J. G. Galaz-Montoya, S. H. Shahmoradian, K. Shen, J. Frydman, W. Chiu, *Communications Biology* **2021**, *4*, 849.

[45] T. R. Peskett, F. Rau, J. O'Driscoll, R. Patani, A. R. Lowe, H. R. Saibil, *Mol. Cell* **2018**, *70*, 588–601.e586.

[46] a) J. Yang, X. Yang, *Front. Genet.* **2020**, *11*, 754; b) R. S. Fisher, R. M. Jimenez, E. Soto, D. Kalev, S. Elbaum-Garfinkle, *Protein Sci.* **2021**, *30*, 1482–1486; c) N. Riguet, A.-L. Mahul-Mellier, N. Maharjan, J. Burtscher, M. Croisier, G. Knott, J. Hastings, A. Patin, V. Reiterer, H. Farhan, *Nat. Commun.* **2021**, *12*, 6579.

[47] a) P. J. B. Pereira, J. A. Manso, S. Macedo-Ribeiro, *Curr. Opin. Struct. Biol.* **2023**, *80*, 102607; b) A. Escobedo, B. Topal, M. B. Kunze, J. Aranda, G. Chiesa, D. Mungianu, G. Bernardo-Seisdedos, B. Eftekharzadeh, M. Gairí, R. Pierattelli, *Nat. Commun.* **2019**, *10*, 2034.

[48] a) T. E. Williamson, A. Vitalis, S. L. Crick, R. V. Pappu, *J. Mol. Biol.* **2010**, *396*, 1295–1309; b) A. K. Thakur, M. Jayaraman, R. Mishra, M. Thakur, V. M. Chellgren, I.-J. L. Byeon, D. H. Anjum, R. Kodali, T. P. Creamer, J. F. Conway, *Nat. Struct. Mol. Biol.* **2009**, *16*, 380–389.

[49] a) A. Patel, H. O. Lee, L. Jawerth, S. Maharana, M. Jahnel, M. Y. Hein, S. Stoynov, J. Mahamid, S. Saha, T. M. Franzmann, *Cell* **2015**, *162*, 1066–1077; b) C. P. Brangwynne, P. Tompa, R. V. Pappu, *Nat. Phys.* **2015**, *11*, 899–904.

[50] K. C. Stein, H. L. True, *Prion* **2011**, *5*, 291–298.
[51] A. B. Meriin, X. Zhang, X. He, G. P. Newnam, Y. O. Chernoff, M. Y. Sherman, *J. Cell Biol.* **2002**, *157*, 997–1004.
[52] D. Kaganovich, R. Kopito, J. Frydman, *Nature* **2008**, *454*, 1088–1095.
[53] F. Aktar, C. Burudpakdee, M. Polanco, S. Pei, T. C. Swayne, P. N. Lipke, L. Emtage, *Life science alliance* **2019**, *2*.
[54] a) R. F. Berkeley, M. Kashefi, G. T. Debelouchina, *Biophys. J.* **2021**, *120*, 1276–1287; b) W. M. Babinchak, R. Haider, B. K. Dumm, P. Sarkar, K. Surewicz, J.-K. Choi, W. K. Surewicz, *J. Biol. Chem.* **2019**, *294*, 6306–6317.
[55] M. H. M. Gropp, C. L. Klaips, F. U. Hartl, *Mol. Cell* **2022**, *82*, 4290–4306 e4211.
[56] H. Park, N. Y. Kim, S. Lee, N. Kim, J. Kim, W. D. Heo, *Nat. Commun.* **2017**, *8*, 30.

Manuscript received: April 29, 2024
Accepted manuscript online: June 16, 2024
Version of record online: July 22, 2024